ELSEVIER

Nuclear Instruments and Methods in Physics Research A 452 (2000) 401–421

NUCLEAR INSTRUMENTS & METHODS IN PHYSICS RESEARCH Section A

www.elsevier.nl/locate/nima

On the reconstruction of Cherenkov rings from aerogel radiators

J. Pinto da Cunha[a,b,*], F. Neves[a,1], M.I. Lopes[a,b]

[a]*LIP-Laboratório de Instrumentação e Física Experimental de Partículas, Department of Physics of the University of Coimbra, 3004-516 Coimbra, Portugal*

[b]*Department of Physics of the University of Coimbra, 3004-516 Coimbra, Portugal*

Received 9 December 1999; received in revised form 25 February 2000; accepted 17 March 2000

Abstract

An event reconstruction algorithm to analyze Cherenkov rings in a Ring Imaging Cherenkov (RICH) detector is considered and the results of a Monte Carlo simulation are discussed. It is demonstrated that aerogel radiators can be used in RICH detectors despite the Rayleigh scattering of light if filtered by a pattern recognition program. The velocity of the particle radiating Cherenkov light, β, is determined by a fit to the photon hit pattern, assuming prior momentum measurement by a tracking system. The charge of the particle, z, is obtained from the collected light. The results show that, for the geometries considered, velocity resolutions $\sigma_\beta/\beta \simeq 1\times10^{-3}$ and charge resolutions $\sigma_Z/Z \simeq 10\%$ can be achieved for 5 GeV/c protons and a 2 cm thick aerogel radiator.

PACS: 29.40.Ka

Keywords: Silica aerogel; Cherenkov counter; Monte Carlo

1. Introduction

Ring Imaging Cherenkov (RICH) counters have been playing an important role in high energy physics and, more recently, in astrophysics experiments [1,2]. A RICH counter can be used to determine both the velocity, β, and the charge, z, of a particle, the latter being obtained by counting the number of Cherenkov photons. By combining the RICH information with the rigidity measurement using a magnetic tracker the particle can be fully identified according to its mass. Moreover, the RICH counter allows very good albedo rejection (i.e. distinguishing upward from downward crossing particles). This is very important, for instance, in astroparticle experiments aiming at the detection of particles coming from space. Such experiments usually have specific constraints that demand the use of non-standard designs to conform to low weight, compactness, low power consumption, etc. Furthermore, due to the limited space available for the experimental setup, the RICH design can be

*Correspondence address: LIP-Laboratório de Instrumentação e Física Experimental de Partículas, Department of Physics of the University of Coimbra, 3004-516 Coimbra, Portugal. Tel.: +239-410-640; fax: +239-829-158.

E-mail address: jpinto@lipc.fis.uc.pt (J. Pinto da Cunha).

[1] Supported by a fellowship from LIP.

0168-9002/00/$ - see front matter
PII: S0168-9002(00)00452-6

highly constrained namely by the presence of other detectors [2–4].

Until recently, RICH counters used NPT gases ($n \gtrsim 1.0015$), NPT liquids (e.g. C_6F_{14}, $n = 1.276$) or crystals (such as NaF, $n = 1.33$), the choice depending on the particles to be identified and their range of momenta [5]. However, in some situations it is desirable to have a radiator with intermediate refractive index, between that of NTP liquid (C_5F_{12}, $n = 1.26$) and the NTP gas (C_4F_{10}, $n = 1.0015$). Hence, some experiments have recently proposed the use of silica aerogel radiators [6–8], a material which can be manufactured with index of refraction ranging typically from 1.01 to 1.2 [9,10]. Although aerogel has been widely used in threshold Cherenkov counters, its use in RICH detectors has been limited by the Rayleigh scattering of light. In fact, aerogel is basically an open structure of $nSiO_2 + 2nH_2O$ globules with dimensions close to the wavelength of the photons, leading to light scattering. The scattered photons eventually reach the photodetectors, producing a background superimposed on the ring patterns of unscattered Cherenkov photons. Therefore, the possibility of using such a radiator relies on the ability to develop techniques that avoid noise from such photons.

Detection of Cherenkov rings generated in aerogel radiators has been reported [11–13]. However, to our knowledge, the contribution of the Rayleigh background to β resolution has not yet been worked out, and no separation of scattered from unscattered photons was described. On the other hand, background subtraction cannot be applied successfully in an event by event basis [11].

The main purpose of this work is to present an algorithm for the reconstruction of RICH rings, particularly suitable for cases where a background of scattered photons is present, and general enough to permit the analysis in case of unconventional geometries. This algorithm is used to study the performance of three different RICH detectors that use aerogel radiators and might be potentially interesting for astrophysical applications.

A general approach to assess the performance of an RICH detector is considered, from both view points of simulation and event reconstruction. The simulation is based on the package GEANT 3.21, available from CERN [14]. The program of simulation is modular enough to allow different geometries to be easily considered and various contributions to be studied separately.

The event analysis comprises a pattern recognition aimed at extracting the signal from the background of photons that underwent multiple scattering and of those due to photons radiated by δ-rays or secondary particles created in hadronic collisions, together with fitting the set of selected photon hit positions that determines the velocity of the particle that produced Cherenkov light. The pattern recognition suppresses most of the scattered photons, while keeping the unscattered ones and allowing velocity effective fitting, even when copious Rayleigh background is present. Furthermore, most of the photons produced by δ-rays and other secondary particles are removed. The charge of the particle is obtained by counting the total number of photons converted in the photodetectors.

In this work only events consisting of one single impinging particle are considered.

2. Simulation

2.1. Detector geometry

Three different RICH designs have been considered, which are schematically depicted in Fig. 1a–c:

(a) The proximity focusing configuration, consisting of a plane radiator slab separated from a detector plane by an empty space in which the Cherenkov rings expand [15].
(b) A geometry derived from the previous one, in which a conical mirror reflects the light towards a matrix of photodetectors located along the lateral wall of a cylinder placed coaxially with the mirror [16].
(c) A geometry containing two conical mirrors in a coaxial arrangement, with photodetectors placed in the area between the two mirror bases.

The geometries (b) and (c) are thought to permit the installation of other detectors after the RICH,

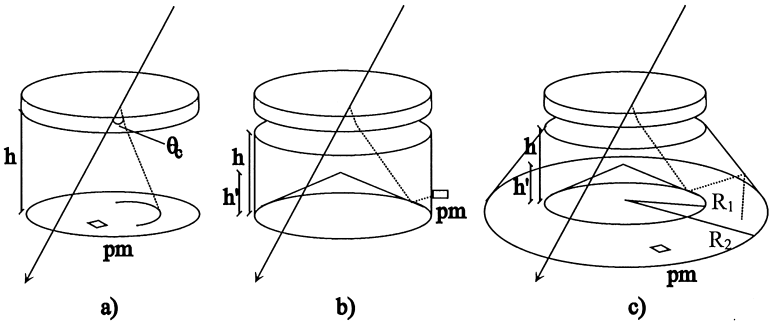

Fig. 1. Geometries of the detectors considered: (a) proximity focused; (b) derived from (a) with a conical mirror and photodetectors on the lateral wall of a cylinder; and (c) a double conical mirror assembly with readout at the lowest plane.

Table 1
Summary of the reference geometrical parameters

		(cm)
Geometry (a)	Radiator radius	50
	Expansion height	40
	Photodetector radius	50
Geometry (b)	Radiator radius	50
	Cylinder radius	50
	Cylinder height	50
	Cone mirror height	10
	Cone radius	50
Geometry (c)	Radiator radius	50
	Internal cone mirror height	10
	Internal cone radius	35
	External mirror height	50
	External mirror base radius	110
	External mirror top radius	50

e.g. a calorimeter, as the corresponding radiation length for a particle crossing the counter is negligible. Additionally, in geometry (c) the photodetectors have been moved away from the top of the Cherenkov counter, where a magnetic tracker is supposed to operate and a fringe field might exist. The dimensions of the radiator were fixed throughout this work as 2 cm thickness and 50 cm radius. The other dimensions were varied to study the influence of the geometrical parameters on the performance of the detectors (cf. Section 5) and are listed in Table 1.

The radiator was assumed to be homogeneous and made of a single piece of material. Therefore, no account was made of effects due to shape or size of any pieces required to build the radiator area. Furthermore, the RICH was supposed to work in vacuum, so no air effects whatsoever were considered.

It was assumed that the momentum of the particles entering the radiator is measured by a tracking system in front of the RICH. The geometric acceptance of the RICH was calculated in the Monte Carlo simulation requiring that the particle crosses the tracker from top to bottom, striking the radiator surface. The tracker was assumed to be cylindrical, with radius 50 cm and height 100 cm. Furthermore, in the calculation of the geometric acceptance, multiple scattering and curvature of the particle trajectory in the tracker due to the magnetic field were neglected as a first approximation.

2.2. Radiator optical properties

The radiator was ascribed the refractive index $n = 1.14$, at $\lambda = 400$ nm. Concerning the optical dispersion, $n(\lambda)$, since there are no published data for silica aerogels, one used the values plotted in Fig. 2 which were obtained by the approximated scaling law

$$n_{\mathrm{aer}}(\lambda) \simeq \frac{\langle n_{\mathrm{aer}} \rangle - 1}{\langle n_{\mathrm{slc}} \rangle - 1} n_{\mathrm{slc}}(\lambda) \quad (1)$$

which is expected to hold for identical molecular structures [12,17,18], where $n_{\mathrm{slc}}(\lambda)$ is the optical dispersion of fused silica [19]. The average was calculated over the range of wavelengths of interest,

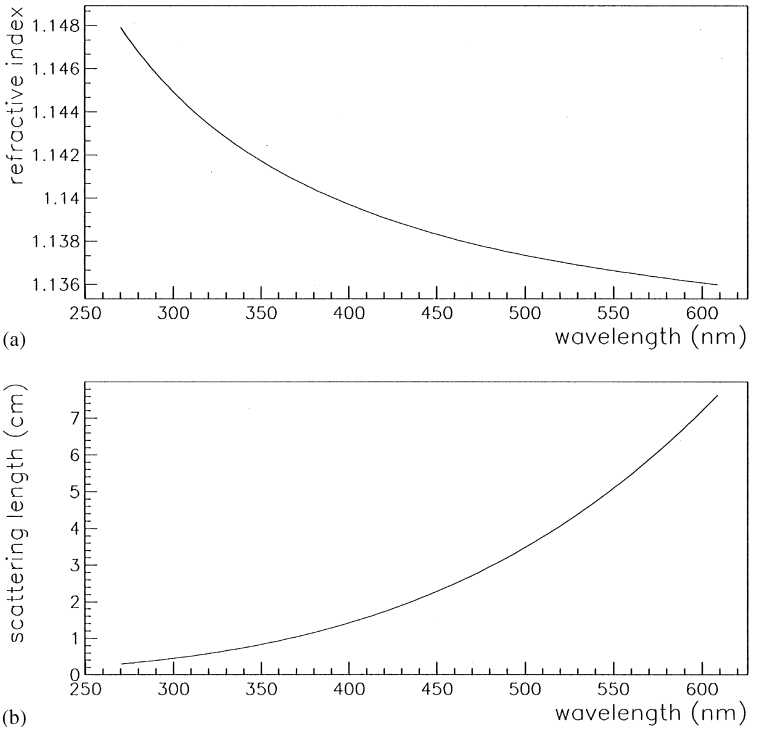

Fig. 2. Optical properties of aerogel as a function of the wavelength: (a) refractive index, scaled from the optical dispersion of fused silica and (b) the Rayleigh scattering length for an aerogel with a clarity coefficient $C = 0.018\ \mu m^4/cm$.

$\lambda \in [270,600]$ nm. This scaling law is consistent within the errors with sparse measurements of laser refraction [7].[2]

The transport of photons in the bulk of the radiator is governed by absorption loss and Rayleigh scattering, the latter process depending on the relative size of the scattering centers and the photon wavelength. The scattering length, Λ_{sc}, is well described by

$$\Lambda_{sc}(\lambda) = \frac{\lambda^4}{C} \tag{2}$$

where C is a constant, frequently referred to as the clarity coefficient of the material and the dependency λ^4 is well known for Rayleigh scattering. Obviously, for the application of aerogel in an RICH detector, the lowest possible value of C is desirable. According to recent publications, aerogels with a clarity coefficient smaller than $0.01\ \mu m^4/cm$ are available [7,11,20,22]. However, it seems that high refractive index aerogels are less transparent [23]. Thus, in the present simulation, a less optimistic value was assumed, setting $C = 0.018\ \mu m^4/cm$ [24]. Fig. 2b shows the scattering length versus photon wavelength for this aerogel, calculated according to Eq. (2).

Concerning the absorption of photons in silica aerogels, recent improvements in the manufacture technique have led to the production of highly transparent materials, although, there are no reliable data on the dependence of the absorption coefficient, Λ_{abs}, on the wavelength. Recent measurements suggest a relation $\Lambda_{abs}(\lambda) = \alpha\Lambda_{sc}(\lambda)$, with $\gtrsim 100$, approximately constant [20,21]. A value $\alpha = 100$ was considered.

[2] We measured the refractive index of a small piece of aerogel from Matsushita, by the minimum deflection of laser light with $\lambda = 632$, 514, and 472. Results showed consistency with the scaling law within errors.

2.3. Event simulation

The computing code, based on the GEANT 3.21 package, is intended to simulate all the processes that take place when a charged particle traverses the radiator and produces Cherenkov light. Thus, the occurrence of hadronic collisions, multiple scattering, the production of δ-rays and their tracking along the radiator were all taken into account. The kinetic energy threshold for tracking electrons and gammas was set to 10 keV. Concerning the transport of Cherenkov photons, GEANT takes into account absorption and boundary processes, using the specified optical properties of the detector media, considering the polarization of the photons. Rayleigh scattering is not treated. Hence, a routine has been implemented to generate coherent Rayleigh scattering of light photons, so that this process could be included in the photon transport. The scattered photon direction is generated according to the cross section [25], with a probability distribution function given by

$$\mathrm{d}P\,\mathrm{d}\vartheta\mathrm{d}\varphi = \tfrac{3}{8}(1+\cos^2\vartheta)\sin\vartheta\,\mathrm{d}\vartheta\,\mathrm{d}\varphi \qquad (3)$$

ϑ and φ being the polar and azimuthal angles relative to the photon initial direction.

The transport of photons is performed in small steps. At each step a length, x_k, is generated for each of the processes, $k = 1,2,\ldots$, being considered, as $x_k = -\Lambda_k \ln(r)$, Λ_k being the mean free path length of process k and r a uniform random number, $r \in [0,1]$. At each step the photon is given the smallest length, $\min(x_k)$, and the corresponding cross section is activated.

The optical properties of the radiators considered are those plotted in Fig. 2 and discussed in the previous section. As for the density of the aerogel, the relation $\rho = 5.263(\langle n\rangle - 1)$ was assumed to hold [26,27]. The Cherenkov photons are followed throughout the detector until they are absorbed in a photodetector (or elsewhere) or escape through the top or the lateral surfaces of the radiator (assumed to be black painted).

The response of the photodetectors was not fully simulated. Only the quantum efficiency was taken into account, being set as typical of a photomultiplier with bialkali photocathode and a borosilicate glass window (see Fig. 3). The reflectivity of the mirrors was assumed to be 85%, independent of the wavelength [29]. Effects due to possible magnetic fringe field were not taken into account.

For each event simulated, the relevant information, namely the coordinates of photon hits in the photodetector matrix, was written to an output file for later analysis. This allowed a detailed event selection and debugging to be carried out.

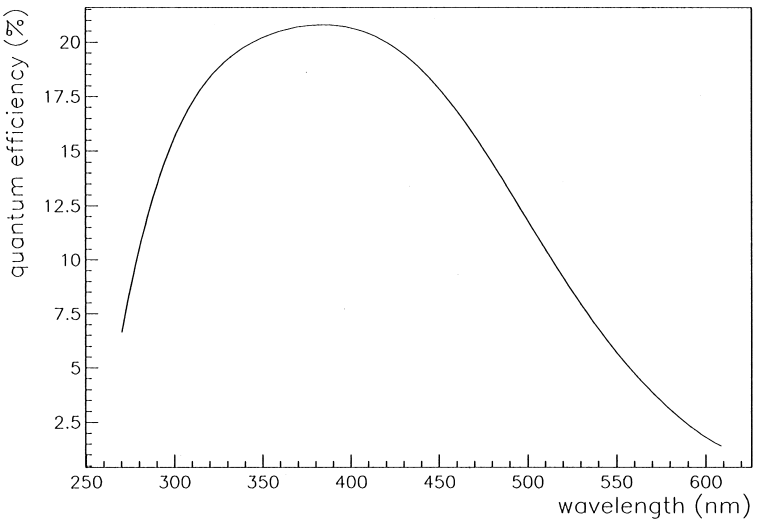

Fig. 3. Quantum efficiency of the Hamamatsu 5900 photomultiplier with bialkali photocathode and a borosilicate glass window.

3. The event reconstruction

The number of Cherenkov photons with wavelength between λ and $\lambda + d\lambda$ generated by a particle of charge z and velocity β per unit of track length in a radiator is given by the Frank–Tamm relation [28]

$$\frac{d^2\mathcal{N}}{d\ell\, d\lambda} = 2\pi\alpha z^2\left(1 - \frac{1}{\beta^2 n^2(\lambda)}\right)\frac{1}{\lambda^2} \quad (4)$$

where α is the fine structure constant and n the refractive index of the radiator. The photons are emitted with an angle relative to particle trajectory given by

$$\cos\theta_c = \frac{1}{\beta n}. \quad (5)$$

Therefore, the photon hit pattern is directly related to the kinematics of the radiating particle. However, the photons are produced all along the particles' track inside the radiator and the angle of emission of each photon λ varies with $n(\lambda)$. Thus, average values are usually considered at the event reconstruction, both for the production point and for the refractive index, since the wavelength and direction of the photons are not measured. These effects, which increase with increasing thickness and chromatic dispersion of the radiator, limit the determination of β.

For the geometries considered in this study, the patterns of photon hits in the detector matrix are not circles, except for the proximity focused detector (geometry (a)) if the particle has normal incidence relative to the radiator plane. For other angles of incidence, the patterns of hits in the detector plane are not true conical sections, due to the refraction at the radiator surface facing the expanding volume. Nonetheless, for this geometry the inverse problem of calculating the Cherenkov angle, θ_c of each individual photon hit has been worked out, assuming that (i) the photon creation point (taken as the middle point of the radiator) and (ii) the refractive index (approximated to $n = \langle n(\lambda)\rangle$) are known for every photon [15].

For more complex designs, namely geometries (b) and (c) considered in this work, the patterns of hits are highly dependent on the incidence direction and impact point of the particle on the radiator. The inverse problem of calculating θ_c can be extremely difficult to obtain and has to be worked out for each particular geometry. Therefore, a general method of reconstruction has been devised that might be used with quite diverse geometries. Furthermore, the events include significant background, specially due to (i) Rayleigh scattered photons, most of which have some correlation with the signal (unscattered photons), and (ii) emission of Cherenkov light by energetic δ-rays, mostly emitted forward relative to the particle's direction. Therefore, a two-level analysis has been implemented for the event reconstruction, consisting of a pattern recognition, aimed at rejecting the background hits, followed by a fit to the hits accepted by the pattern (signal).

The reconstruction of the event is meant to determine β. Usually this is obtained from the average value of θ_c considering every detected photon [15]. However, it is clear that θ_c has a functional dependence on λ, i.e. $\theta_c = \theta_c[\beta, n(\lambda)]$ and, therefore, β should be used, rather than θ_c, as the parameter in the fit to the set of data points consisting of the photon hit positions. Moreover, as $\beta \in [0,1]$, the domain of parameter search is defined independent of the dispersion relation.

3.1. Pattern recognition

The pattern recognition is based on matching the set of data points and a theoretical curve, $\boldsymbol{\zeta}$, which depends on $\boldsymbol{\beta} = \beta\hat{\beta}$, the velocity of the radiating particle, whose direction $\hat{\beta}$ is given by the tracking system. The hit points not consistent with $\boldsymbol{\zeta}$ are rejected. Besides, curve $\boldsymbol{\zeta}$ is also a function of λ, the photon generation point along the particle's track, $\boldsymbol{s}$, and ϕ_c, the azimuthal angle in the particle's rest frame, i.e. $\boldsymbol{\zeta} = \boldsymbol{\zeta}(\boldsymbol{\beta}, \lambda, \boldsymbol{s}, \phi_c)$. The curve $\boldsymbol{\zeta}$ represents the set of positions on the photodetector surface that might be illuminated by unscattered Cherenkov photons, as ϕ_c varies from 0 to 2π. This function was calculated analytically for each geometry, taking into account the refraction at the interface between the radiator and the expansion volume and the reflections at all surfaces met by the photon. Our purpose is to adjust β in order to match the maximum number of data points.

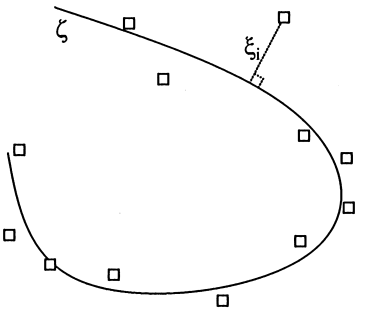

Fig. 4. The event reconstruction algorithm is based on finding the smallest set of distances, ξ_i, to the predicted curve, $\boldsymbol{\zeta}$, which is a function of β. The parameter β is varied so that the distances are minimized.

Nonetheless, as λ and $\boldsymbol{s}$ vary continuously within a certain range, it is necessary to consider a set of discrete values of λ and $\boldsymbol{s}$, so that the above function be suitable for fitting β. This has been done by defining λ_k and $\boldsymbol{s}_\ell$ points, with $k = 1, \ldots, k_M$ and $\ell = 1, \ldots, \ell_M$ (spaced according to the statistics given by the Monte Carlo).[3] The simplest case is to ascribe average values to λ and $\boldsymbol{s}$, resulting in a single $\boldsymbol{\zeta}$ function. With k_M and ℓ_M points one has a family of $k_M \times \ell_M$ curves for a given β. Usually it is enough to set $k \gtrsim 3$ and $\ell \gtrsim 3$. For each data point i, ξ_i is chosen such that $\xi_i = \min\{\xi'_{k\ell}(i)\}$, where $\xi'_{k\ell}(i)$ is the smallest distance of hit i to curve $\boldsymbol{\zeta}_{k\ell}$ (see Fig. 4).

Having calculated the set $\{\xi_i\}$ we can start a fitting procedure by minimizing, in β, the sum $\chi[\beta]$, defined as

$$\chi[\beta] = \sum_{i=1}^{N} |\xi_i| \tag{6}$$

where the sum is evaluated over all the N photon hits of the event, and ξ_i is given as above, for each photon hit position, $\boldsymbol{r}_i$ (taken as the center of each photodetector pixel).

[3] The Monte Carlo distributions referred to in the text are $dN/d\lambda$ and $dN/d\ell$, where ℓ is the depth throughout the radiator, ranging from zero to the thickness. $dN/d\ell$ is not constant because of absorption and scattering effects, and $dN/d\lambda$ does not exhibit $1/\lambda^2$ behaviour due to λ-dependent scattering processes.

The pattern recognition algorithm follows the following prescription:

1. Set $k = 1$ and $\ell = 1$ to get a single curve, $\boldsymbol{\zeta}$. Calculate $\chi[\beta]$, and minimize in order to obtain the best value of β in first approximation, i.e. $\beta_0 = \beta$: $\chi = \min\{\chi[\beta]\}$.
2. By using $\beta = \beta_0$ and a family of 3×3 curves, calculate the set of $\{\xi_i\}$, $i = 1, \ldots, N$, such that $\xi_i = \min\{\xi'_{k\ell}(i)\}$, as defined above.
3. Form the histogram $\{\xi_i\}$ and look for clusters.
4. Cut at the boundary of the main cluster.
5. Keep the set of selected points for further analysis.

With the previous description we get quite sharp separation between signal and noise, by clustering $\{\xi_i\}$ and disregarding those ξ_i sitting away from the main cluster. Applying this method with a family of 3×3 curves, we find a rejection of 95% of noise hits due to Rayleigh scattered photons and 90% photons produced by secondary particles, loosing only 2% of good hits (see Fig. 5).

It should be stressed that the main cluster in the distribution of ξ refers to the $\{\xi_i\}$ that gather together near zero for the signal hits. This cluster does not necessarily correspond to close groups of hits in the event display (Fig. 5).

This method can be readily applied to every geometry provided the correct function $\boldsymbol{\zeta}$ is calculated for each case. Hence, mechanical uncertainties in the placement of detector parts can be included.

It is worth noting that the use of absolute values in defining χ is preferable to the more common use of the sum of squares. This happens because, prior to noise elimination, signal and noise are added together in χ sum, which leads to over-contributions (in comparison with a simple sum) from far away points (i.e. the background) if squares are used, so that the curve at χ minimum is biased relative to signal points.

The algorithm described above can easily be applied to the analysis of events containing more than one particle by repeating the method on the set of formerly rejected points, provided the corresponding particles have been tracked and their momenta measured.

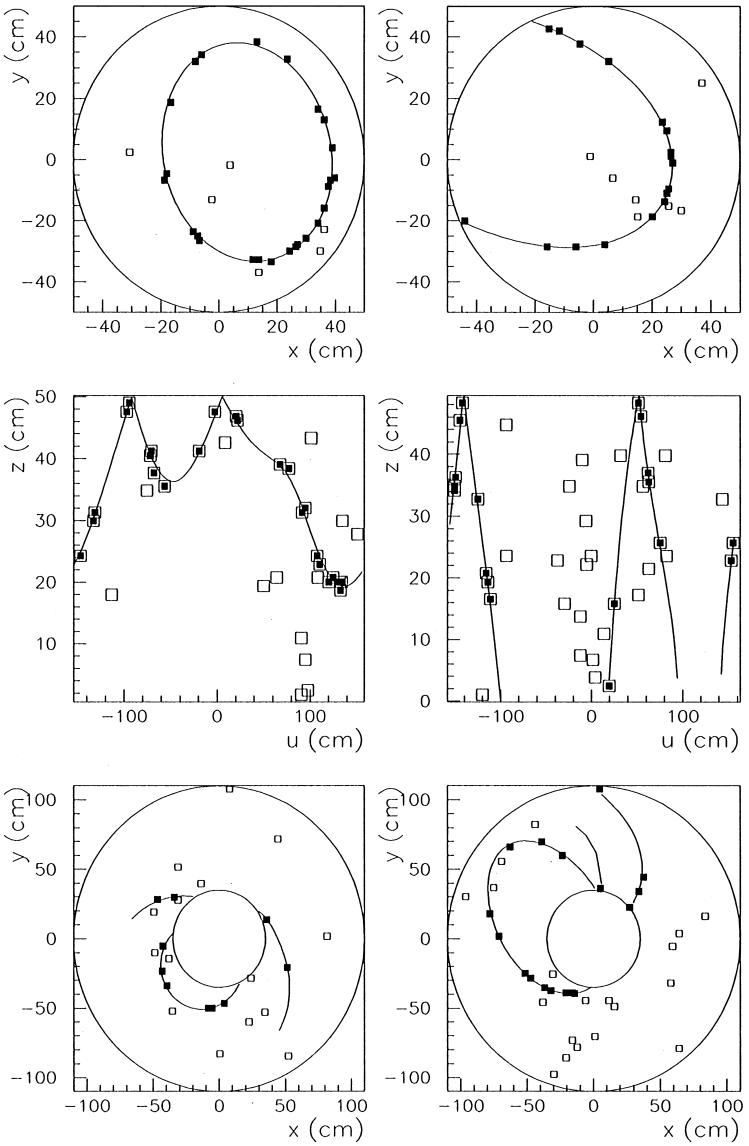

Fig. 5. Display of patterns of hits for geometries (a) top row, (b) middle row and (c) bottom row. The solid points represent the hits selected by the pattern recognition. The curves resulted from the fit to the set of selected hits. In geometry (b) the variable $u = R\tan^{-1}(y/x)$, where R is the radius of the cylinder and (x, y) the coordinates of the hit point. Each plot displays one event only. As can be seen, the rings are highly dependent on the kinematics of the incident particle, specially for the latter two geometries.

3.2. β determination

The velocity of the particle, β, is obtained from a fit to the set of selected points, with the function ζ referred above, varying β so that $\chi^2 = \sum_{i=1}^{N} \zeta_i^2$ is minimized. The uncertainty in the measurement of β, β_f, is estimated as usual from the width of the χ^2 well at the minimum, $\chi^2_{\min}$, i.e. σ_β: $\chi^2(\beta_f \pm \sigma_\beta) = \chi^2_{\min} + 1$.

Fig. 5 displays some reconstructed events due to 5 GeV/c protons with different incidence directions and impact points. It is clear that the hit patterns

have very different contours when the impact parameters are changed. The pattern recognition and the fitting have to cope with such a variety of shapes.

4. Particle charge determination

Neglecting multiple scattering of the particle in the radiator, the number of photoelectrons produced in the matrix of photodetectors of an RICH can be written from Eq. (4) as

$$N_{\mathrm{pe}} = G(\vartheta,\varphi,\boldsymbol{r}_{\mathrm{p}},\beta)\,2\pi\alpha\frac{Lz^2}{\cos\vartheta}\int\left(1-\frac{1}{\beta^2 n^2(\lambda)}\right)\frac{1}{\lambda^2}Q(\lambda)A(\lambda)f(\lambda)\,\mathrm{d}\lambda \tag{7}$$

where L is the thickness of the radiator, $Q(\lambda)$ the quantum efficiency of the photodetectors, $A(\lambda)$ a factor that accounts for the absorption of photons in the radiator and $f(\lambda)$ takes into consideration losses due to reflection of light at the lower surface of the radiator, i.e. the light trapped by total reflection. The geometrical factor, $G(\vartheta,\varphi,\boldsymbol{r}_{\mathrm{p}},\beta)$, accounts for the incomplete collection of transmitted photons due to light absorbed in mirrors (if they exist) or reflected back to the radiator, existence of dead areas and lateral escape of photons from the expansion volume, in the case of the proximity focused geometry without mirrors. G thus depends on the velocity, incidence direction (ϑ,φ) and impact point of the particle on the radiator, $\boldsymbol{r}_{\mathrm{p}}$.

The dependence of G on the velocity of the particle arises from the variation of the aperture of the Cherenkov cone on β with consequences for the light collection. Therefore, N_{pe} can be written as $N_{\mathrm{pe}} = \mathscr{A}(\vartheta,\varphi,\boldsymbol{r}_{\mathrm{p}},\beta)z^2$ where $\mathscr{A}$ is a function characteristic of a given RICH detector.[4]

The charge of the particle can be determined from the number of photoelectrons, provided that the function $\mathscr{A}(\vartheta,\varphi,\boldsymbol{r}_{\mathrm{p}},\beta)$ is known. Thus, for a specific radiator, the charge determination requires the reconstruction of β, as well as the knowledge of the momentum vector and impact point of the incident particle on the radiator. These are obtained by extrapolating into the radiator the particle trajectory reconstructed in the tracker.

It is very difficult to obtain accurate enough analytical/numerical expressions of $\mathscr{A}(\vartheta,\varphi,\boldsymbol{r}_{\mathrm{p}},\beta)$, for the geometries studied in the present work. Hence, the charge determination is based on a look-up-table (LUT) of values for each detector geometry. Given the axial symmetry of the detectors considered, the number of entries of the LUT can be reduced to 4, i.e. $(\vartheta,\varphi,\varrho,\beta)$, with $\vartheta\in[0,\vartheta_{\max}]$, $\varphi\in[0,\pi]$, β above the threshold, and $\varrho\in[0,R_{\mathrm{rad}}]$, where ϱ is the distance of the impact point to the center of the radiator upper surface, R_{rad} being the radius of the radiator slab and $\vartheta_{\max}\simeq\pi/4$ the maximum value of ϑ given by the geometrical acceptance of the detector. Reducing the number of dimensions of the LUT permits a major reduction in the LUT size and in the filling statistics.

The values of $\mathscr{A}$ were obtained by simulating the response of the detector to incident protons covering the range of ϑ, φ, ϱ and β, according to the intervals listed above and for a fixed value of the polar angle, ψ, of impact point in the upper surface of the radiator relative to its center ($\psi=0$ was chosen). The LUT was filled with the value $N_{\mathrm{pe}}(\vartheta,\varphi,\boldsymbol{r}_{\mathrm{p}},\beta)$ of each event of an entire event sample. The values in the table were then used to calculate the charge of the radiating particle (assumed unique) of any event of other samples with $(\vartheta,\varphi,\varrho,\beta)$ and producing N_{pe} photoelectrons, as

$$z=\sqrt{\frac{N_{\mathrm{pe}}}{\mathscr{A}(\vartheta,\varphi',\varrho,\beta)}} \tag{8}$$

where $\varphi'=|\varphi-\psi|$, and if $|\varphi-\psi|>\pi$ then $\varphi'=2\pi-|\varphi-\psi|$. When reading from the LUT, $\mathscr{A}(\vartheta,\varphi',\varrho,\beta)$ is obtained by linear interpolation of neighbor values.

As the response of the photodetectors was not simulated (apart from the quantum efficiency), it was assumed that the number of photoelectrons, N_{pe}, can be given approximately by the number of photodetector hits. This assumption is a reasonable first approach to the problem of the z determination for light isotopes, for which the number of

[4] It is frequent to consider the approximation $\sin\theta_{\mathrm{c}}\approx$ constant in the interval of integration, in which case $N_{\mathrm{pe}} = N_0 Lz^2\sin^2\theta_{\mathrm{c}}$, where N_0 is called the figure of merit of the detector.

photoelectrons produced in a pixel per event is seldom larger than 1. A step forward should consider the simulation of the response of the photodetectors. Thus a better determination of the number of photoelectrons can be obtained from the sum of the signals of all fired photodetectors in one event.

5. Results

The simulation output was analyzed in detail both to understand the simulation results and to identify the most relevant issues affecting the performance of the detector. Therefore, we considered contributions from various physical processes to the photon output. For this purpose we considered 5 GeV/c protons striking perpendicularly to the radiator surface. The results of the simulation show that about 17.1% of the protons produce δ-rays with energy above the Cherenkov threshold. This value has been confirmed by explicitly calculating the number expected, based on the cross section for δ-ray production [30,31],

$$\frac{\mathrm{d}N}{\mathrm{d}x}\Big|_{T>T_c} = \frac{D}{2}z^2\frac{Z}{A}\frac{\rho}{\beta^2} \times\left[\left(\frac{1}{T_c}-\frac{1}{T_M}\right)\frac{\beta^2}{T_M}\ln\left(\frac{T_c}{T_M}\right) + \frac{T_M - T_c}{2(p^2+M^2)}\right] \tag{9}$$

with

$$T_M = \frac{2m\beta^2\gamma^2}{1+2\gamma m/M+(m/M)^2}$$

and

$$D = 0.3071\ \text{MeV cm}^2/\text{g} \tag{10}$$

where T_c is the electron kinetic energy at the Cherenkov threshold and T_M is the maximum kinetic energy that can be transferred to the electron (of mass m) by the particle of mass M, charge z, momentum p, velocity β and Lorentz factor γ, in a medium with Z/A and density ρ. This formula leads to the production of 0.191 δ-rays above threshold per crossing of 2 cm aerogel, by a 5 GeV/c proton. This means that in these circumstances the probability of getting an event with energetic δ-rays, is 17.4%, which compares to 17.1% from the simulation. However, when looking at the converted light we find only 12% of the events having photons produced by δ-rays, since part of these photons does not reach the photodetectors. This class of events shows abundant photon yield, so that in average 18% of the photons detected originate in δ-rays. Concerning the Rayleigh scattering, we find that approximately 50% of all photons produced undergo Rayleigh scattering. Therefore, this scattering has a major effect on the photon hit pattern at the photodetector planes, by smearing the ring patterns of unscattered photons. The contributions from other processes are much less important. Table 2 shows the percentages of events having Cherenkov photons radiated by other but the incident particle.

Table 2
Contributions of the various physical processes for the production of Cherenkov photons. Percentage of events having photons originating in secondary particles for the process shown

Process	%
δ-rays	11.9
Hadronic collisions	1.5
Other processes	$\lesssim$0.1

Concerning light collection, we find about 40 photoelectrons in average, for $\sim$460 photons generated in the radiator by 5 GeV/c protons. Dependencies on the polar angle of incidence, impact point and momentum are shown in Fig. 6.

5.1. β resolution

Unless stated otherwise, the results presented in this section were obtained with 5 GeV/c protons ($\beta = 0.983$) with an angular distribution given by the geometrical acceptance of the detector (see Section 2.1) and the set of geometrical parameters listed in Table 1. Furthermore, it was assumed that the photodetectors do not have photon counting capability. Hence, only one hit is assigned to a photodetector, independent of the number of photoelectrons produced. Since no specific

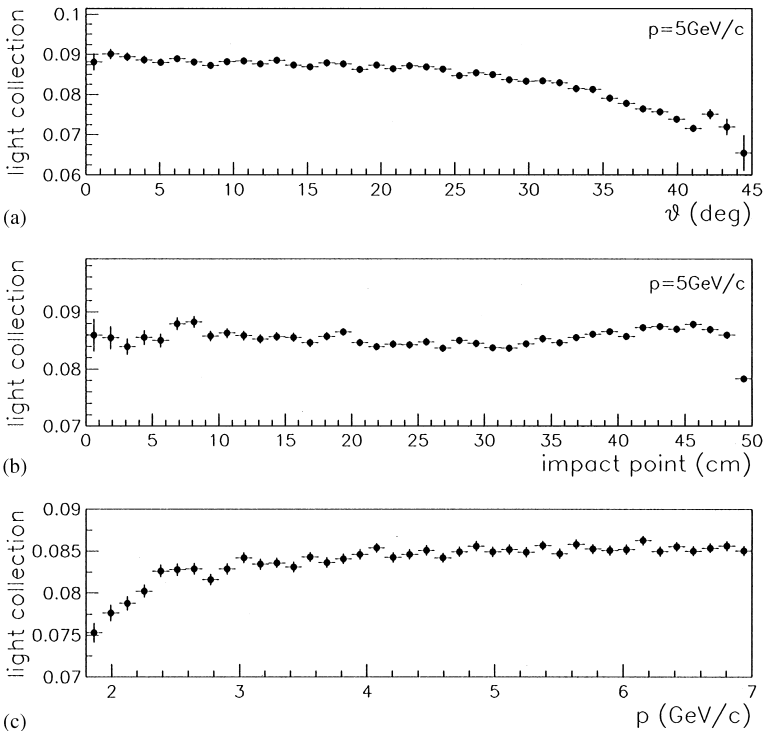

Fig. 6 . Light collection efficiency as a function of (a) incident angle, (b) impact point and (c) momentum.

photodetector is assumed, the photon losses in dead zones were not considered in this study, although their effect will be estimated below.

Uncertainties in the fitted β come from various sources, namely: (a) intrinsic limitations of the algorithm of reconstruction; b) the uncertainty in the photon emission point (discussed in Section 3.1); (c) the chromatic dispersion in the radiator, $n(\lambda)$; (d) backgrounds, especially (i) detected photons that had undergone Rayleigh scattering, and (ii) detected photons that were radiated by δ-rays and other secondary particles produced in the radiator; (e) photodetector pixel size.

The contribution of the various sources to β resolution was studied. The physical processes were activated selectively in the simulation and no pattern recognition filters were applied. Hence, distributions of $\Delta\beta/\beta$ were obtained under the following conditions at the simulation level: (a) "*pure signal*", i.e. constant refractive index, no δ-rays generated, no Rayleigh scattering included, no hadronic collisions, etc.; (b) as (a) plus the effect of the chromatic dispersion; (c) as (b) plus the inclusion of processes leading to the production of secondary particles in the radiator; (d) all physical effects (chromaticity, Rayleigh scattering and production of photoelectrons by secondary particles) are included. The results are represented in Fig. 7a–d. As expected, the main degradation of β comes from the Rayleigh scattering.

Fig. 8 shows $\Delta\beta/\beta$ when the pattern recognition is applied, for geometries (b) and (c). We conclude that the pattern recognition algorithm eliminates the tails and improves the resolution to values approaching those obtained in the absence of Rayleigh scattering and radiating δ-rays. For this work only events having at least 6 photon hits were reconstructed (99.7% of the events), for which the reconstruction is successful in 99.8% of the cases. Therefore, the overall reconstruction efficiency is 99.5% of the events.

Henceforth, the results shown were obtained including in the simulation all the physical effects discussed above.

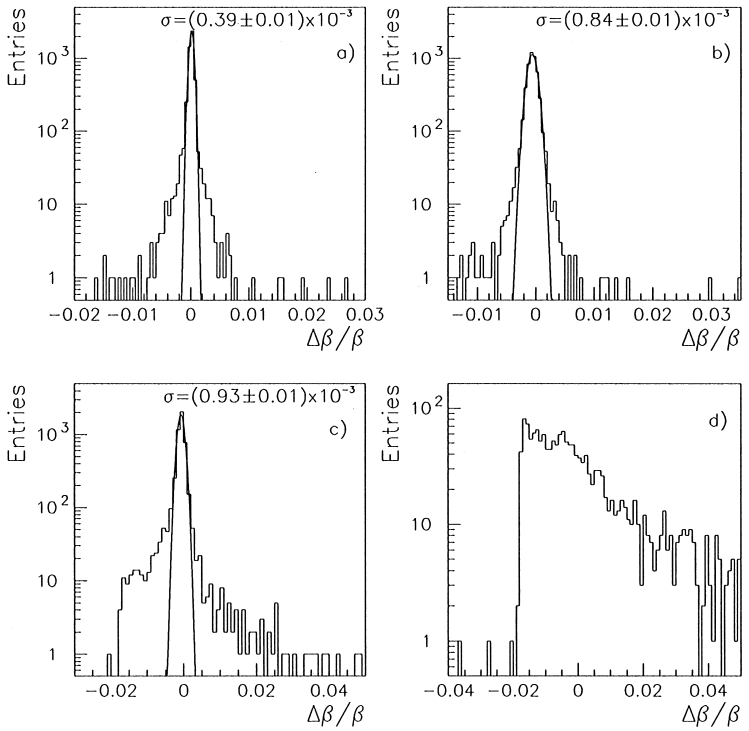

Fig. 7. Contribution of different physics processes to $\Delta\beta/\beta$: (a) "*pure signal*", i.e. no optical dispersion, no δ-rays, no Rayleigh scattering; (b) as (a) plus the effect of the chromatic dispersion; (c) as (b) plus the inclusion of physical processes yielding secondary particles in the radiator; (d) all physical effects (chromaticity, Rayleigh scattering and production of photoelectrons by secondary particles) are included. These curves refer to geometry (c). Results are similar for the other geometries considered. No pattern recognition is applied.

The results presented in Fig. 7a–d do not take into account the size of the photodetector pixel. This was investigated and the effect of pixel size on the β resolution is illustrated in Fig. 9. As a compromise between keeping the resolution as good as possible and a moderate number of photodetectors, the pixel size was set equal to 7 mm^2 in the reconstructions presented henceforward. Fig. 10 shows the distribution of $\Delta\beta/\beta$ obtained, for the geometries with mirrors, when the pattern recognition is applied and all effects included.

The resolution $\Delta\beta/\beta$ is shown in Fig. 11 for protons as a function of the momentum for geometry (c). The resolution degradation at low momentum is due to the reduction in photon yield. The same behavior was observed for geometry (b).

The variation of $\Delta\beta/\beta$ with the polar angle of incidence and the distance of the impact point of the particle on the radiator to the center is plotted in Fig. 12. Each data point is an average over the azimuthal angle of incidence, according to the acceptance of the detector discussed in Section 2.1. Clearly, the resolution deteriorates somewhat for high angles and more peripheral impact points, in all cases.

The dependence on the height of the mirror is shown in Fig. 13 for geometry (b). It is evident that smaller mirrors give a better resolution because the hit points are much scattered in comparison with a higher mirror, hence increasing the ring definition and the photon statistics by reducing the number of photodetectors receiving more than one photon. The results for geometry (c) are more difficult to present graphically, because the number of varying parameters is high. Typical values of $\Delta\beta/\beta$ for different combinations of the geometric parameters are shown in Table 3.

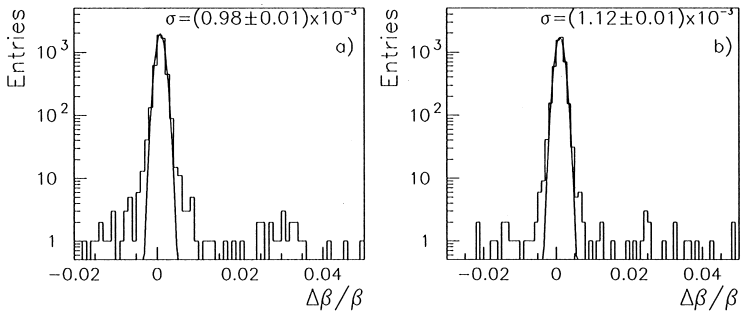

Fig. 8. Distribution of $\Delta\beta/\beta$, for geometries (b) and (c) (at right), upon application of the pattern recognition. The background influence is highly reduced.

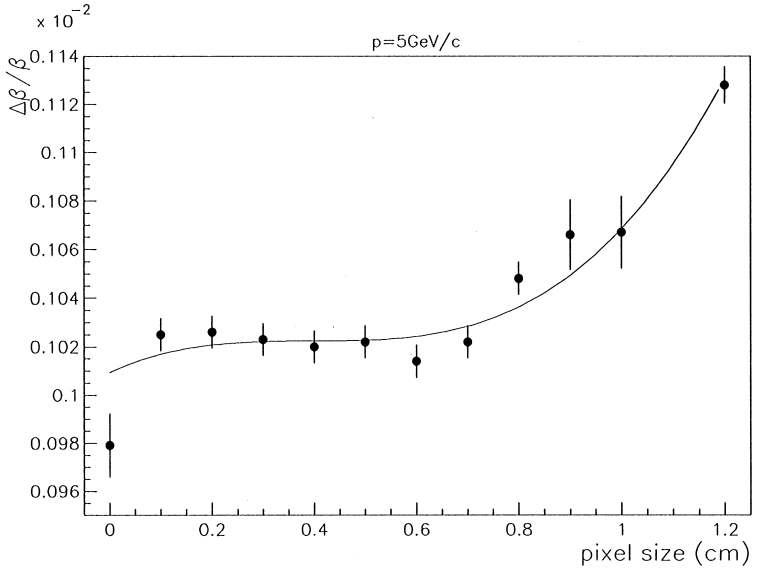

Fig. 9. $\Delta\beta/\beta$ for different values of the pixel size. A pixel of 7×7 mm^2 was chosen.

As a way of estimating how photon losses might affect the resolution, e.g. due to possible dead zones in the photodetectors, etc., the light collection efficiency of the photodetectors was decreased. The effect on $\Delta\beta/\beta$ is shown in Fig. 14.

Aerogels produced recently have clarity coefficients much lower than previous ones. In this work a less favorable case was assumed. Nonetheless, a more transparent aerogel with clarity coefficient $C = 0.01$ μm^4/cm was studied and it was concluded that the Rayleigh scattered photons are still an important limiting factor to the ring reconstruction. Therefore, the methods aforementioned may certainly be useful also in this case (see Fig. 15). However, it should be noted that there have been reports of aging of aerogel samples [32], making it advisable to be more conservative with respect to the optical performance of this material.

For the sake of comparison, we present in Fig. 16 the resolutions $\Delta\beta/\beta$ given by the method proposed above and the average method due to Ypsilantis [15], for the case of a proximity focused geometry. In the latter case we are limited by the tails due to background hits, though, for each event, values of

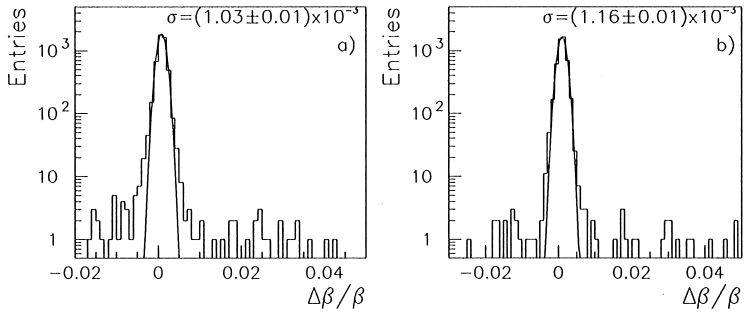

Fig. 10. Distribution of $\Delta\beta/\beta$, for geometries (b) and (c) (at right), for a pixel size of 7×7 mm^2, upon application of the pattern recognition.

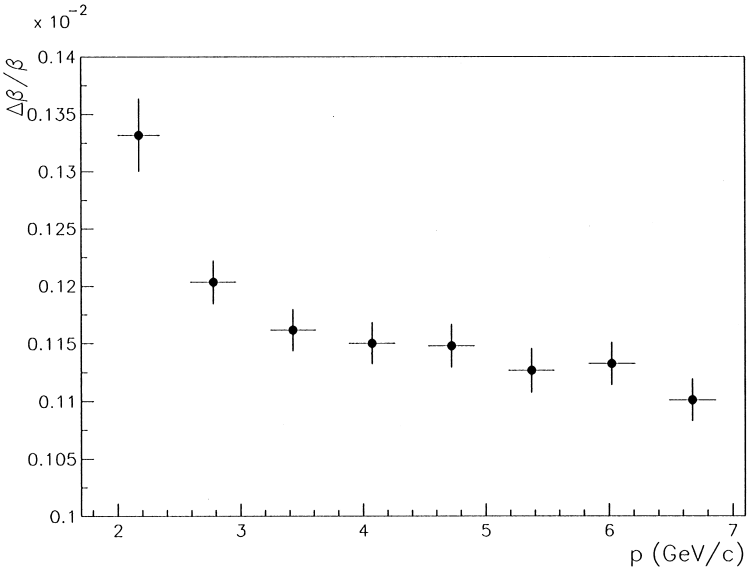

Fig. 11. Distributions of $\Delta\beta/\beta$ as a function of momentum.

θ_c aside the main cluster of Cherenkov angles had not been considered in the average, $\langle\theta_c\rangle$. Therefore, we conclude that the method described in Section 3.1 can be more effective in the case of presence of background.

5.2. z determination

Fig. 17 shows the distribution of z, determined by the method described in Section 4, for 5 GeV/c protons with an angular distribution given by the acceptance of the detector (see Section 2.1), and the set of parameters listed in Table 1 for geometry (b). The right-hand-side tail of the distribution is due to events in which there are many photoelectrons originated from δ-rays and other secondary particles produced in hadronic collisions. These events give rise to a number of photoelectrons much larger than the mean value kept in the LUT for the same conditions regarding the incident particle. They are also responsible for the shift of the mean value of the distribution towards a value smaller than 1, due to an "artificial" increase of the mean values of the LUT (during the fill-in). Both effects were investigated by analyzing samples of events having no secondary particles. The result is plotted in Fig. 17 (dashed line).

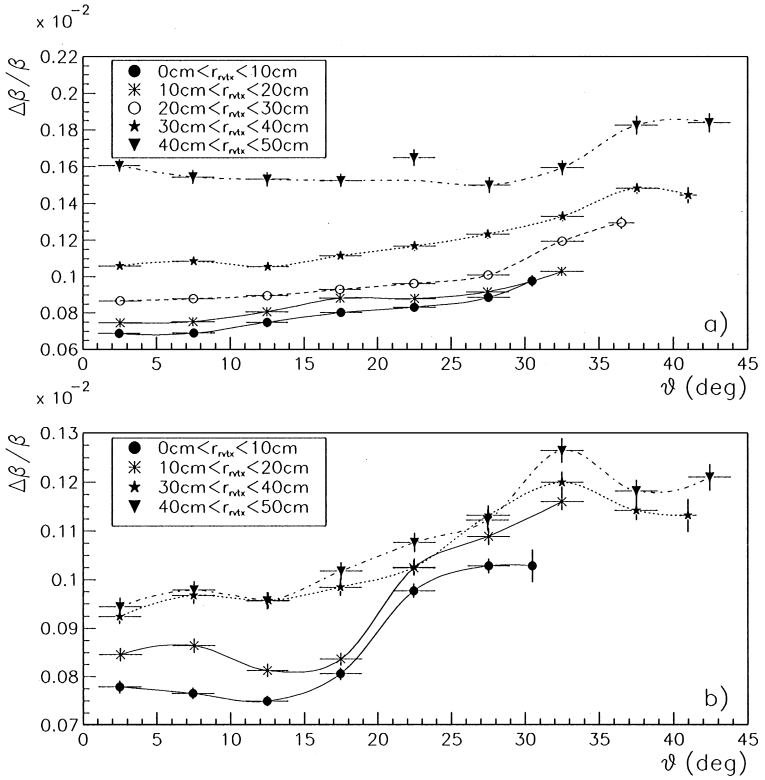

Fig. 12. Distributions of $\Delta\beta/\beta$ as a function of polar angle of the incident particle, for geometries (b) top and (c).

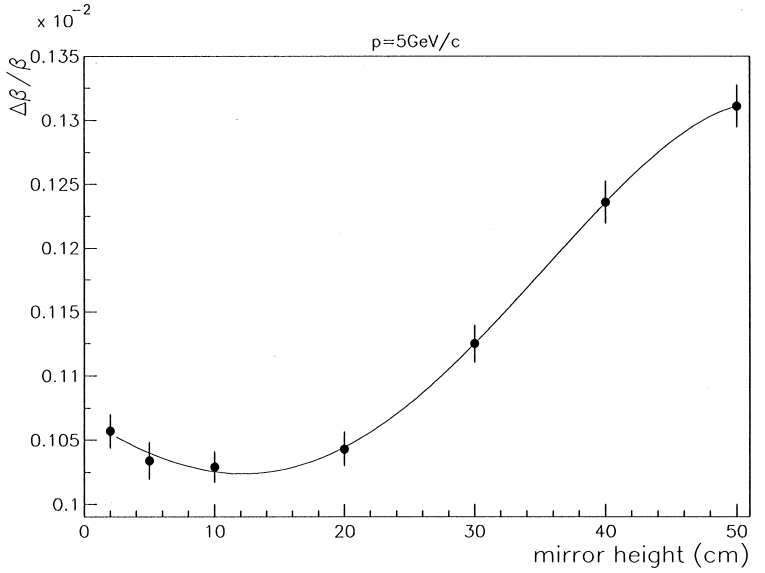

Fig. 13. Distributions of $\Delta\beta/\beta$ as a function of the height of the cone mirror in geometry (b).

Table 3
Resolution $\Delta\beta/\beta$ for various dimensions in geometry (c). Dimensions are in centimeters

R_1 (cm)	h_1 (cm)	R_2 (cm)	h_2 (cm)	$\Delta\beta/\beta$ ($\times 10^{-3}$)
35	18	70	40	1.49 ± 0.02
35	18	70	25	1.71 ± 0.03
35	18	90	40	1.33 ± 0.02
35	18	90	25	1.64 ± 0.03
35	18	120	40	1.28 ± 0.02
35	40	90	45	1.35 ± 0.02
50	18	90	40	1.69 ± 0.03
35	30	110	40	1.34 ± 0.02
35	20	110	40	1.30 ± 0.02
35	10	90	40	1.31 ± 0.02
35	10	110	30	1.50 ± 0.02
35	10	110	50	1.15 ± 0.02
50	10	110	50	1.37 ± 0.02

Fig. 18 shows the determination of the charge for nuclei with $z < 5$ and momentum/nucleon equal to 5 GeV/c, for geometry (b). A systematic shift of the central values for $z > 1$ is a consequence of the difference between the multiplicities for protons and for other nuclei, since the charges are obtained comparing the number of photoelectrons against proton filled LUT contents.

With the purpose of eliminating background photons we might construct an LUT considering the points selected by the pattern recognition procedure only (see Section 3.1). In so doing, we expect to reject most of the noise coming from energetic δ-rays. However, this would be done at the expense of reducing the statistics of photons that underwent Rayleigh scattering, thus introducing additional statistical fluctuations. The results show that the width of the z distribution is larger due to statistical reduction, but the tail corresponding to δ-rays and

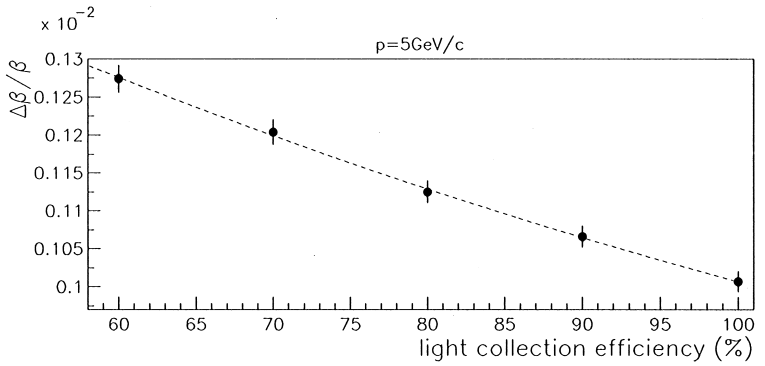

Fig. 14. The resolution $\Delta\beta/\beta$ as a function of the light collection efficiency.

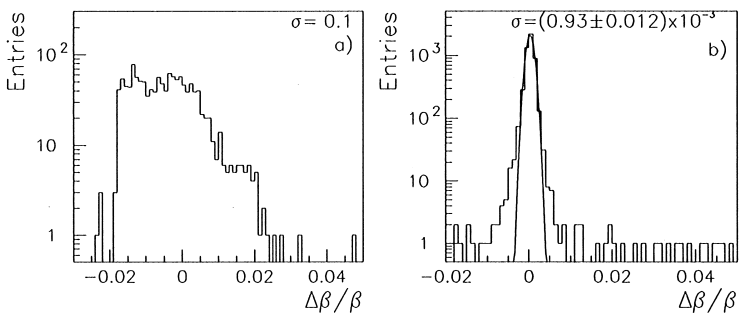

Fig. 15. $\Delta\beta/\beta$, for an aerogel radiator of clarity coefficient $C = 0.01$ μm^4/cm, and geometry (b), when all effects are included: (a) without and (b) with pattern recognition.

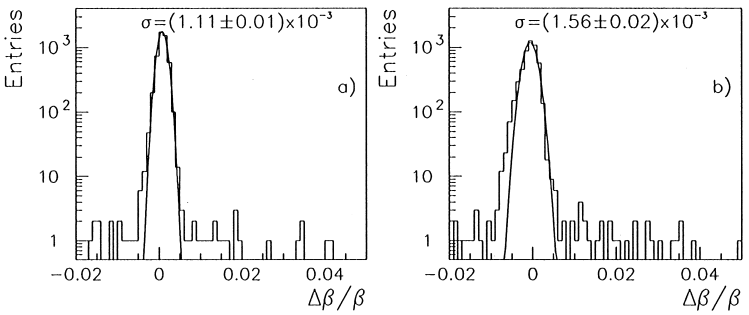

Fig. 16 . Distributions of $\Delta\beta/\beta$ for a proximity focused geometry using (a) the fit method discussed in this work and (b) the average θ_c method.

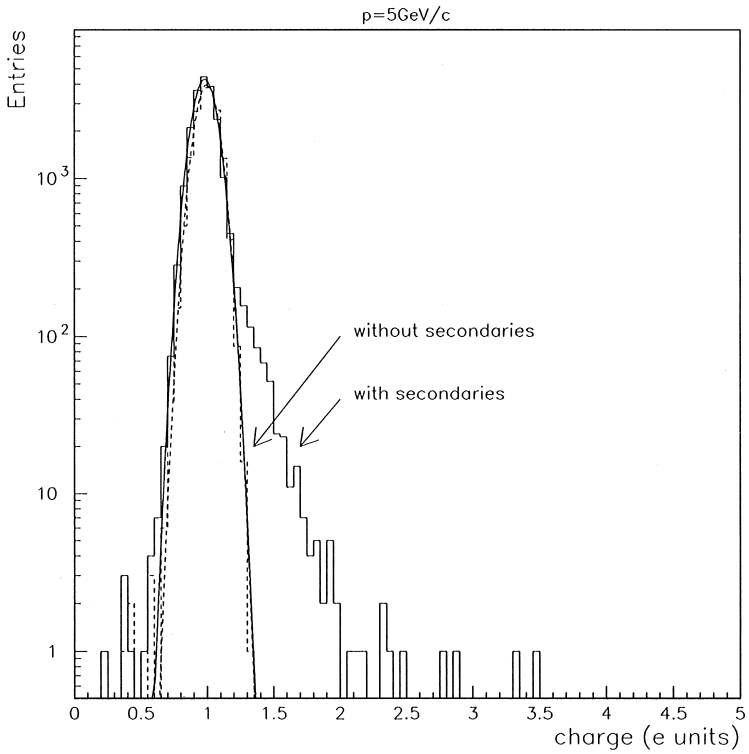

Fig. 17. Distribution of z for 5 GeV/c protons with an angular distribution given by the acceptance of the detector: all effects included (solid line); production of secondary particles or δ-rays suppressed (dashed line).

other secondaries is greatly reduced (see Fig. 19). The helium curve has a small tail on the left-hand side originated by badly reconstructed events, but those can be removed from the final sample by looking at the quality of the fit. The percentage of protons above a given cut in z is plotted in Fig. 20 for various values of the cut, with and without pattern recognition of photon hits. Hence, when the pattern recognition algorithm is used for z determination, we increase the rejection of protons in an He sample, although loosing $\approx 1\%$ more of helium nuclei.

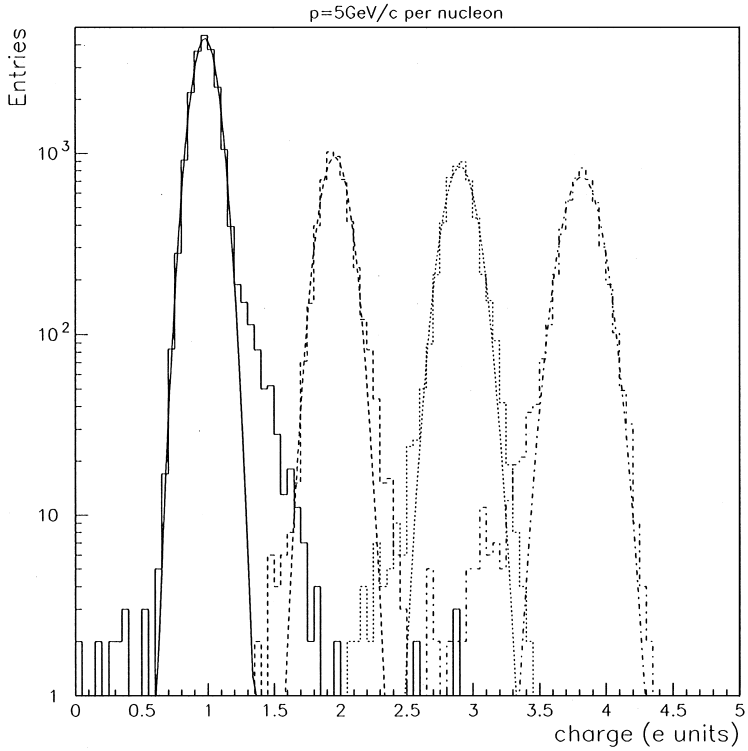

Fig. 18. Distribution of z for nuclei with $z < 5$ and momentum 5 GeV/c per nucleon, for geometry (b).

In Fig. 21 we plot the contamination of protons in the He sample, for a flux of protons 7 times higher than the flux of He, a value frequently quoted in the literature for the composition of cosmic rays at the top of the atmosphere [33]. As it can be seen, the contamination is significantly decreased by using only pattern selected photons in the z determination.

The systematic shift observed in Fig. 18 is also remedied, at least in part, by the pattern recognition. In fact, referring to Fig. 19, the central values show no significant bias for $z > 1$ particles as a consequence of having reduced the number of photons that enter in the calculation of z, thus decreasing the multiplicity effect mentioned above. The right-hand-side shoulder for $z = 3$ is a consequence of decreasing the pattern recognition efficiency with increasing the photon yield.

In the above discussion we did not consider the quality of the β fit, as we intended to apply the method to all events. Nevertheless, badly reconstructed events can be removed from the final sample. Referring to Fig. 22, we can remove the tails in $\Delta\beta/\beta$ and in z if a cut at 3% CL is applied. In this procedure we lose about 12% and 4% of protons and He, respectively.

6. Conclusions

We have demonstrated the possibility of using aerogel as an RICH radiator, even if Rayleigh scattering is significant, and outlined the influences of many processes on the β and z measurements.

An algorithm for pattern recognition has been implemented aimed at rejecting the Rayleigh scattered photons and part of the photons produced by secondary particles and energetic δ-rays. The filter is selective enough to allow keeping most of the signal (unscattered photons).

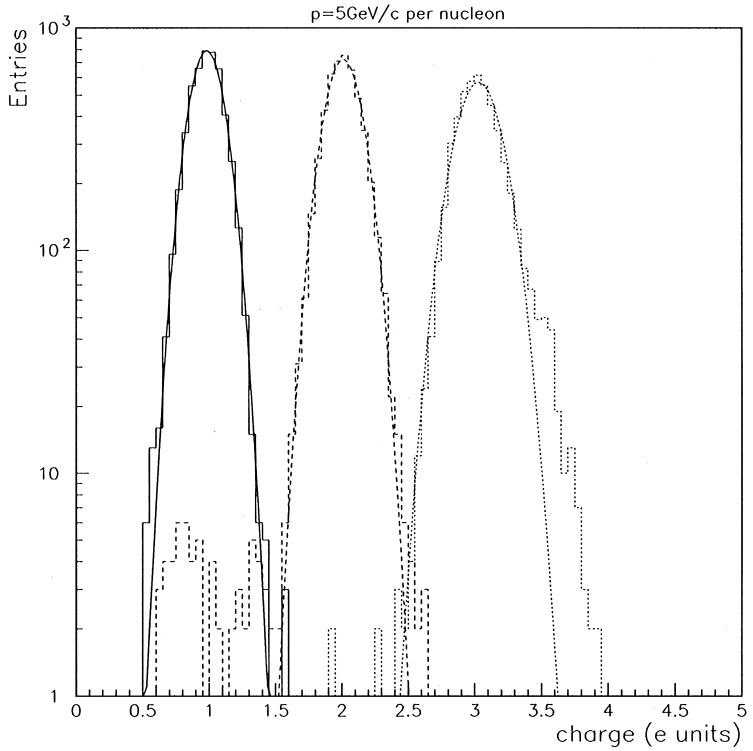

Fig. 19. Distribution of z for nuclei with $z < 5$ and momentum 5 GeV/c per nucleon if only pattern selected photons are used to determine the charge, for geometry (b).

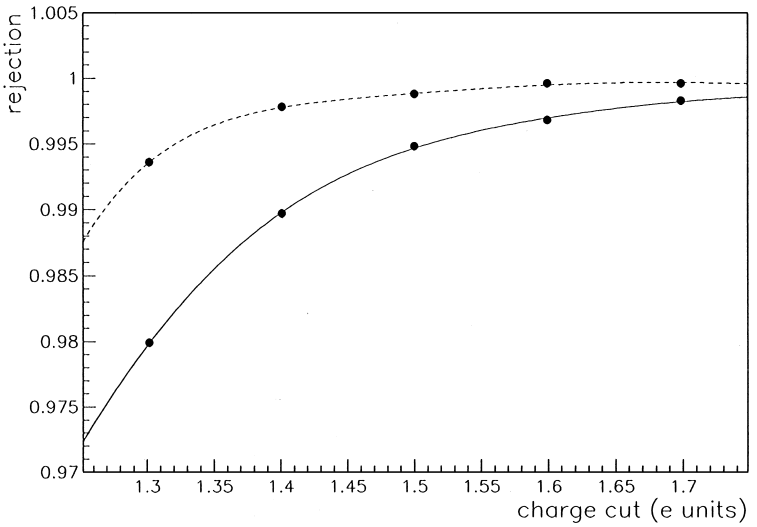

Fig. 20. Rejection curves for p/He separation if all photon hits are used (solid line); if only unscattered photons are counted (dashed curve).

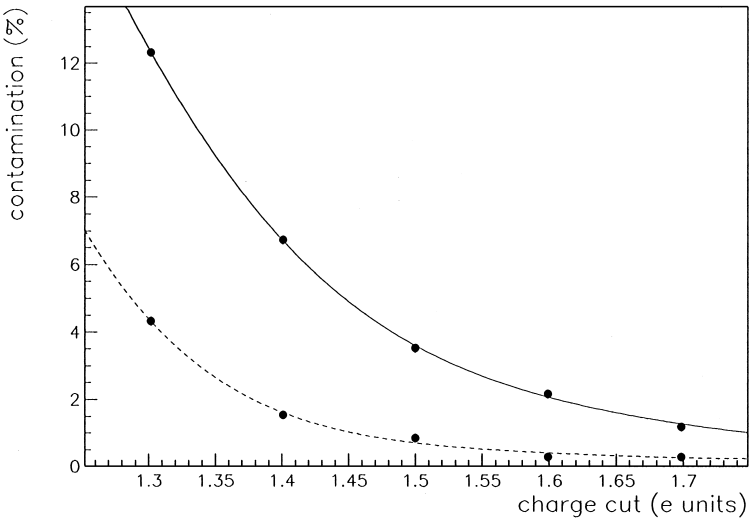

Fig. 21. Contamination of protons in a sample of helium for a ratio of fluxes 7:1, as a function of the cut, if (a) all photon hits are used (full line), and (b) only unscattered photons are counted (dashed line).

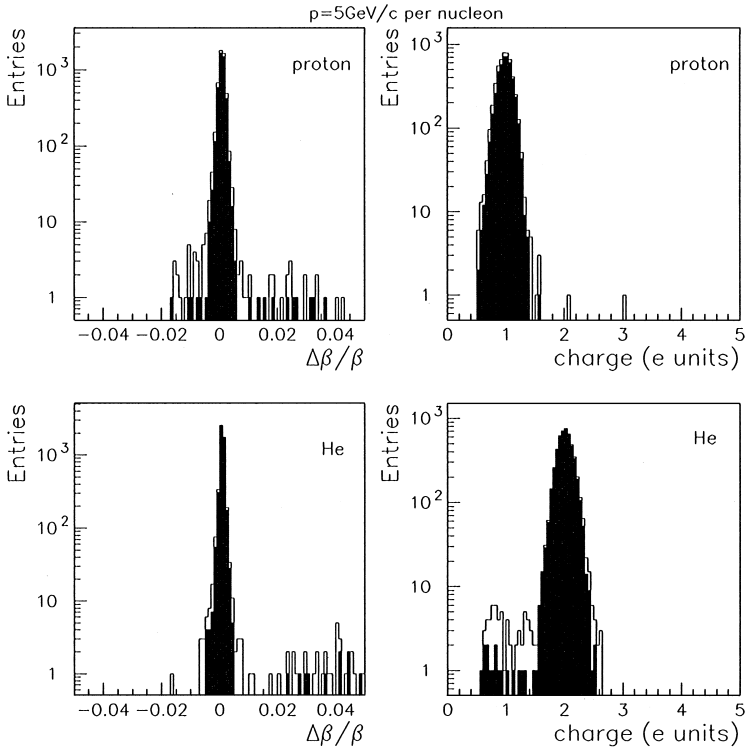

Fig. 22. Distributions of $\Delta\beta/\beta$ and z for protons and He. The hatched areas are for events with more than 3% CL.

The fit to the selected set of photon hits proved to be very effective after background has been removed, enabling good β and charge determination, even when complicated geometry designs are considered and the Cherenkov photons undergo multiple reflections. This approach treats the event as a whole, contrary to other techniques which reconstruct the Cherenkov angle for each detected photon hit point (one at a time) and take the average as the best angle.

The methods were applied to the charge determination allowing good p/He separation, despite energetic δ-rays and other secondary particles producing Cherenkov photons.

The methods described in this work have the advantage of allowing the analysis of events having more than one radiating particle, both in velocity and charge. Furthermore, the use of two radiators of different refractive indices in front of each other might be easily accounted for since the photon generation points and optical dispersions are inputted into the reconstruction (see Section 3.1).

Work is underway in order to improve the simulation by considering more realistic reflectivities, the roughness of the mirror surfaces, modeling of mechanical uncertainties, the photodetector response and the momentum resolution as given by the tracking system.

The codes are written in ANSI Fortran 77 and the sources are available from the authors upon request.

Acknowledgements

This work was developed within the framework of the AMS Collaboration, and has been financed by the project CICT/ALPOI/CERN/DIV/1179 from ICCTI, Portugal. In the course of this work we benefited from discussions with colleagues from the RICH group of AMS Collaboration, especially with Prof. G. Barreira. We are grateful to Profs. R. Ferreira Marques and N. Ayres de Campos for reading the manuscript.

References

[1] P. Carlson et al., Nucl. Instr. and Meth. A 349 (1994) 577.
[2] V.M. Balebanov et al., Alpha Magnetic Spectrometer (AMS) Proposal 1995.
[3] R. Bellotti et al., Phys. Rev. D 60 (1999) 052002.
[4] J.W. Mitchell et al., Phys. Rev. Lett. 76 (1996) 3057.
[5] T. Ekelöf, Nucl. Instr. and Meth. A 433 (1999) 372.
[6] The LHC-B Letter of Intent, CERN/LHCC 95-5, 1995.
[7] P. Carter, Nucl. Instr. and Meth. A 433 (1999) 392.
[8] The Belle Detector Tecnical Design Report, KEK, 1995.
[9] M. Cantin et al., Nucl. Instr. and Meth. A 118 (1974) 177.
[10] I.L. Rasmussen, Rev. Phys. Appl. C 4 (1989) 221.
[11] R. De Leo et al., Nucl. Instr. and Meth. A 401 (1997) 187.
[12] Z. Ren et al., Nucl. Instr. and Meth. A 433 (1999) 172.
[13] R. Forty, Nucl. Instr. and Meth. A 384 (1996) 167.
[14] R. Brun et al., GEANT User's Guide, CERN DD/EE/82.
[15] T. Ypsilantis, J. Seguinot, Nucl. Instr. and Meth. A 343 (1994) 30.
[16] F. Barão, Proceedings of the Second International Workshop on New Worlds in Astroparticle Physics, World Scientific, Singapore, 1999.
[17] M. Born, E. Wolf, Principles of Optics, Pergamon Press, Oxford, 1980.
[18] S. Henning, L. Svensson, Phys. Scripta 23 (1981) 697.
[19] M. Brassed (Ed.), Handbook of Optics, Vol. II, McGraw Hill, New York, 1995.
[20] R. Suda et al., Nucl. Instr. and Meth. A 406 (1998) 213.
[21] G. Poelz, Nucl. Instr. and Meth. A 248 (1986) 118.
[22] E. Albrecht et al., Nucl. Instr. and Meth. A 411 (1998) 249.
[23] Matsushita Electric Works, Ltd., private communication.
[24] D.E. Fields et al., Nucl. Instr. and Meth. A 349 (1994) 431.
[25] J.D. Jackson, Classical Electrodynamics, 2nd Edition, Wiley, New York, 1975.
[26] A.R. Buzykaev et al., Nucl. Instr. and Meth. A 433 (1999) 396.
[27] P. Wang et al., J. Phys. D 27 (1994) 414.
[28] I.M. Frank, I. Tamm, C.R. Acad. Sci. USSR 14 (1937) 109.
[29] A. Braem et al., Nucl. Instr. and Meth. A 320 (1992) 228.
[30] B. Rossi, High Energy Particles. Prentice-Hall, Inc., Englewood Cliffs, NJ, 1952.
[31] Particle Data Group, Phys. Rev. D 54 (1996) 134.
[32] D.W. Higinbotham, Nucl. Instr. and Meth. A 414 (1998) 332.
[33] M.S. Longair, High Energy Astrophysics, Cambridge University Press, Cambridge, 1981.